

See discussions, stats, and author profiles for this publication at: <https://www.researchgate.net/publication/9002034>

Novel Microporous Lanthanide Silicates with Tobermorite-Like Structure

ARTICLE in JOURNAL OF THE AMERICAN CHEMICAL SOCIETY · NOVEMBER 2003

Impact Factor: 12.11 · DOI: 10.1021/ja036988p · Source: PubMed

CITATIONS

53

READS

74

5 AUTHORS, INCLUDING:



Artur Ferreira

University of Aveiro

72 PUBLICATIONS 1,740 CITATIONS

SEE PROFILE



Duarte Ananias

University of Aveiro

80 PUBLICATIONS 1,730 CITATIONS

SEE PROFILE



Luís D Carlos

University of Aveiro

483 PUBLICATIONS 9,774 CITATIONS

SEE PROFILE



Joao Rocha

University of Aveiro

455 PUBLICATIONS 9,830 CITATIONS

SEE PROFILE

Novel Microporous Lanthanide Silicates with Tobermorite-Like Structure

Artur Ferreira,[†] Duarte Ananias,[‡] Luís D. Carlos,[§] Cláudia M. Morais,[‡] and João Rocha^{*,‡}

Contribution from the Department of Chemistry, CICECO, University of Aveiro, 3810–193 Aveiro, Portugal, ESTGA, CICECO, University of Aveiro, 3810-193 Aveiro, Portugal, and Department of Physics, CICECO, University of Aveiro, 3810–193 Aveiro, Portugal

Received July 1, 2003; E-mail: ROCHA@DQ.UA.PT

Abstract: The synthesis and structural characterization of microporous lanthanide silicates ($\text{Na}_{1.08}\text{K}_{0.5}\text{Ln}_{1.14}\text{Si}_3\text{O}_{8.5}\cdot 1.78\text{H}_2\text{O}$, Ln = Eu, Tb, Sm, Ce) are reported. The structure of these solids is closely related with the structure of hydrated calcium silicate minerals known as tobermorites and was solved by powder X-ray diffraction *ab initio* (direct) methods and further characterized by chemical analysis, thermogravimetry, scanning electron microscopy, ^{23}Na and ^{29}Si MAS NMR and luminescence spectroscopy. These materials combine microporosity with interesting photoluminescence properties, and their structural flexibility allows fine-tuning of luminescence properties, by introducing a second type of lanthanide ion in the framework. Thus, they may find applications in new types of sensors.

Introduction

Conventional zeolites are well-known crystalline hydrated aluminosilicates with open framework structures built of $[\text{SiO}_4]^{4-}$ and $[\text{AlO}_4]^{5-}$ tetrahedra linked to each other by sharing all the oxygen to form regular pores and channels of molecular dimensions.¹ These materials are of considerable technological importance as shape-selective catalysts, ion-exchange solids, and molecular sieves. At present, there is a considerable interest in silicate materials which possess zeolite-type structures and contain *stoichiometric* amounts of metal atoms (Ti, Zr, V, Nb, Sn, etc.) in different coordination geometries.² The most prominent family of such solids encompasses microporous titanosilicates, for example ETS-10 and derivatives, containing Ti^{4+} usually in octahedral coordination.^{3,4}

The chemistry of these novel mixed tetrahedral-octahedral (or pentahedral) microporous silicates has been recently extended to the lanthanide elements.^{5,6} Although research into zeolites made luminescent by lanthanide-doping is not new, the preparation of zeolite-type lanthanide silicates is an emerging field. These novel materials are important because they combine in a single, stable, solid microporosity and tunable optical properties, ranging from visible⁶ and infrared^{7,8} luminescence

to X-ray scintillation,⁸ and may find applications in new types of sensors. A few interesting examples of photoluminescent non-siliceous microporous materials, such as rare-earth dicarboxylates and europium hybrid compounds, have also been reported.^{9,10}

There are at least two ways of introducing lanthanide (Ln) ion centers in microporous silicates. The straightforward approach is to ion exchange the cations, such as Na^+ or K^+ , residing in the micropores by Ln^{3+} cations. An example of this is the inclusion of Eu^{3+} in the pores of titanosilicate ETS-10.¹¹ However, in general, the luminescence of the hydrated extraframework Ln^{3+} cations is quenched or partially quenched. Another, more interesting, route is to embed the Ln^{3+} cations into the microporous framework. The resultant silicates contain stoichiometric amounts of lanthanide elements. So far, examples of this approach include only two systems: synthetic analogues ($\text{Na}_4\text{K}_2\text{Ln}_2\text{Si}_{16}\text{O}_{38}\cdot x\text{H}_2\text{O}$) of mineral montregianite,^{5,6} and a new open framework cerium silicate, $\text{Na}_{4.8}\text{Ce}_2\text{Si}_{12}\text{O}_{30}\cdot 4\text{H}_2\text{O}$.¹² Here, we wish to report a new and very promising microporous lanthanide silicate system (AV-20 materials), exhibiting photoluminescence properties, whose structure is closely related with the structure of a fascinating group of minerals known as tobermorites. These hydrated calcium silicate materials are important, for example, in cement hydration and as cation exchangers.¹³

[†] ESTGA, CICECO, University of Aveiro.

[‡] Department of Chemistry, CICECO, University of Aveiro.

[§] Department of Physics, CICECO, University of Aveiro.

- (1) Szostak, R. *Molecular Sieves*; Van Nostrand Reinhold: New York, 1989.
- (2) Rocha, J.; Anderson, M. W. *Eur. J. Inorg. Chem.* **2000**, 801.
- (3) Kuznicki, S. M. *US Pat.*, 485,320.2, 1989.
- (4) Anderson, M. W.; Terasaki, O.; Ohsumi, T.; Philippou, A.; Mackay, S. P.; Ferreira, A.; Rocha, J.; Lidin, S. *Nature* **1994**, 367, 347.
- (5) Rocha, J.; Ferreira, P.; Carlos, L. D.; Ferreira, A. *Ang. Chem. Int. Ed.* **2000**, 39, 3276.
- (6) Ananias, D.; Ferreira, A.; Rocha, J.; Ferreira, P.; Rainho, J. P.; Morais, C. M.; Carlos, L. D. *J. Am. Chem. Soc.* **2001**, 123, 5735.
- (7) Rocha, J.; Carlos, L. D.; Ferreira, A.; Rainho, J. P.; Ananias, D.; Lin, Z. *Mater. Sci. Forum*, in press.

- (8) Ananias, D.; Rainho, J. P.; Ferreira, A.; Rocha, J.; Carlos, L. D. *J. Alloys Compd.*, in press.
- (9) Serpaggi, F.; Luxbacher, I.; Cheetham, A. K.; Férey, G. *J. Solid State Chem.* **1999**, 145, 580.
- (10) Serpaggi, F.; Férey, G.; Antic-Fidancev, E. *J. Solid State Chem.* **1999**, 148, 347.
- (11) Rainho, J. P.; Carlos, L. D.; Rocha, J. *J. Luminescence* **2000**, 87–89, 1083.
- (12) Jeong, H.-K.; Chandrasekaran, A.; Tsapatsis, M. *Chem. Commun.* **2002**, 2398.
- (13) Komarneni, S.; Roy, D. M. *Science* **1983**, 221, 647.

Experimental Section

A. Synthesis. The syntheses of AV-20 materials were carried out in Teflon-lined autoclaves (volume 37 cm³, filling rate 0.62), under static hydrothermal conditions, in ovens preheated at 230 °C. In all of the syntheses, the autoclaves were removed and quenched in cold water after an appropriate time. The off-white microcrystalline powders were filtered, washed at room temperature with distilled water, and dried at 100 °C.

1. Typical Eu-AV-20 Synthesis. An alkaline solution was made by mixing 5.75 g sodium silicate solution (27% m/m SiO₂, 8% m/m Na₂O, Merck), 16.51 g H₂O, 3.25 g KOH (Merck), 1.07 g NaOH (Merck). An amount of 1.37 g of EuCl₃·6H₂O (Aldrich) was added to this solution, and the mixture was stirred thoroughly. The gel, with composition 0.79 Na₂O:1.10 K₂O:1.0 SiO₂:0.07 Eu₂O₃:35 H₂O was autoclaved under autogenous pressure for 3 d at 230 °C. Ce-, Sm-, and Tb-AV-20 were synthesized with substitution of EuCl₃·6H₂O by the LnCl₃·6H₂O, Ln = Ce, Sm, Tb (Aldrich). Mixed Eu/Tb-AV-20 and Tb/Gd-AV-20 were prepared by introducing in the parent gel equimolar amounts of the two lanthanides. EDS analysis, performed on 10 crystals, gave Eu/Tb and Tb/Gd ratios of 0.96–1.02 and 0.94–1.03, respectively. No crystals rich in an individual lanthanide were found. In addition, Rietveld refinement of the mixed lanthanide samples did not allow the determination of partial Ln occupancies. All results indicated that lanthanides are randomly distributed in the crystals.

Within experimental error, chemical analysis by ICP-AES of Eu-AV-20 confirmed the Eu:K:Na:Si molar ratios obtained by powder XRD, ca. 1:0.44:0.93:2.63. Thermogravimetry revealed a total weight loss between 26 and 300 °C of ca. 6.7% (Eu, Sm-AV-20) and 6.9% (Ce-AV-20) corresponding, respectively, to 1.74–1.75 water molecules per formula unit. Eu-AV-20 materials do not adsorb N₂, but the H₂O adsorption isotherms are of Type I (according to the IUPAC classification, $d < 2$ nm), characteristic of microporous solids with a negligible external surface area and maximum H₂O uptakes of 5 mmol × g_{solid}^{-1} . Powder XRD shows that the structure of AV-20 materials is stable up to 800 °C. SEM shows that Eu-AV-20 consists of microcrystalline pseudo-hexagonal thin plates with a lateral dimension of <20 μm.

B. Measurements. SEM images were recorded on a Hitachi S-4100 microscope. EDS was carried out using a EDS Römteck System with polymeric window attached to the scanning electron microscope. ICP analysis was performed by C. A. C. T. I.—Laboratorio Análisis Instrumental, University of Vigo, Spain. Thermogravimetric (TGA) curves were measured with a Mettler TG50 Thermobalance. The samples were heated under air at a rate of 5 °C/min.

Powder X-ray diffraction (XRD) data were collected on a X'Pert MPD Philips diffractometer (CuK_α X-radiation) with a curved graphite monochromator, a fix divergence slit of 1/8°, and a flat plate sample holder, in a Bragg–Brentano para-focusing optics configuration. Intensity data were collected by the step counting method (step 0.03° and time 50 s) in the range 6–140° 2θ.

²³Na and ²⁹Si NMR spectra were recorded at 105.85 and 79.49 MHz, respectively, on a (9.4 T) Bruker Avance 400 spectrometer. ²⁹Si magic-angle spinning (MAS) NMR spectra were recorded with 40° pulses, spinning rates of 5.0 kHz and 50 s recycle delay. Chemical shifts are quoted in ppm from TMS. Single-quantum ²³Na MAS NMR spectra were measured using short and powerful radio frequency pulses (0.6 μs, equivalent to a 15° pulse angle), spinning rates of 14 kHz (Sm, Ce-AV-20) and 28 kHz (Eu-AV-20) and a recycle delay of 2 s. Chemical shifts are quoted in ppm from 1 M aqueous NaCl. The triple-quantum (3Q) ²³Na MAS NMR spectrum was recorded using the Z-filter three-pulse sequence. In this experiment the excitation of the 3Q coherences and its conversion into 0Q coherences, achieved by applying two strong τ f pulses, are followed by a soft $\pi/2$ pulse (the so-called Z-filter). The symmetrization of pathways (0Q → ±3Q → 0Q) allows the simultaneous acquisition of the echo and anti-echo signals with equal intensity, leading to pure absorption spectra. The phase cycling

was composed of 6 phases for the selection of ±3Q coherences. This phase cycling was combined with a classic overall four-phase cycle in order to minimize phase and amplitude mis-settings of the receiver. The lengths of the first and second hard pulses (radio frequency magnetic field amplitude $\nu_1 = 230$ kHz) were 2.5 and 1.0 ms, respectively. The length of the third soft pulse ($\nu_1 = 10$ kHz) was 13 ms. The MAS rate was $\nu_R = 29.7$ kHz. 56 points were acquired in the t1 domain in increments of $(1/\nu_R) = 33.7$ ms. The recycle delay was 1 s, and 2400 scans were recorded for each t1 value. The ppm scale was referenced to ν_0 frequency in the ν_2 domain and to 3.78 ν_0 in the ν_1 domain (ref 1 M aqueous NaCl).

The adsorption isotherms were measured on a C. I. Instruments electrobalance MK2-M5 connected to a vacuum manifold line. Each sample (ca. 0.1 g) was dehydrated overnight at 450 °C to an ultimate pressure of 10^{−4} mbar and then cooled to room temperature.

The visible spectra (10–300 K) were recorded on a Jobin Yvon–Spex spectrometer (HR 460) fitted with a 1200 grooves mm^{−1} grating blazed at 500 nm—coupled to a R928 Hamamatsu photomultiplier. A 150 W Xe arc lamp coupled to an excitation monochromator Jobin Yvon–Spex (TRIAx 180) fitted with a 1200 grooves mm^{−1} grating blazed at 330 nm was used as excitation source. All spectra were corrected for the response of the detectors. The time-resolved measurements were carried out using a pulsed Xe arc lamp (5 mJ/pulse, 3 μs bandwidth) coupled to a Kratos monochromator (GM-252) and a Spex 1934 C phosphorimeter.

Results and Discussion

The powder XRD pattern of Eu-AV-20 was indexed with the PowderX package¹⁴ using the well-resolved first 27 lines. A monoclinic unit cell with $a = 6.851$, $b = 22.248$, $c = 6.828$ Å, $\beta = 113.92^\circ$ was indicated by the TREOR90 indexing program¹⁵ and confirmed with DICVOL.¹⁶ The program Chekcell¹⁷ suggested three possible space groups: $C2$ (No. 5), Cm (No. 8), and $C2/m$ (No. 12).

The ab initio crystal structure determination from powder XRD data was carried out with the EXPO package.¹⁸ After preliminary structural studies with EXPO, the Cm space group was chosen. First, the structure factor amplitudes were extracted by the Le Bail method from the powder pattern.¹⁹ The structure factors of 800 reflections were obtained. Then, the structure was solved by direct methods. Although all atoms were located simultaneously, re-labeling of atoms was necessary, coupled with changes in bond distances and bond angles. This procedure was alternated with least-squares refinements. At this point, it was found that the structure of Eu-AV-20 is closely related with the structure of tobermorite 11 Å (d_{002} XRD peak at 11.3 Å) minerals proposed by Merlino et al.²⁰ Thus, it was decided to change the space group setting from Cm to $B11m$.

The coordinates of atoms obtained from direct methods were used in the Rietveld refinement of the structure by the FullProf

(14) Dong, C. *J. Appl. Crystallogr.* **1999**, 32, 838.

(15) Werner, P. E.; Eriksson, L.; Westdahl, M. *J. Appl. Crystallogr.* **1985**, 18, 367.

(16) Boulit, A.; Louër, D. *J. Appl. Crystallogr.* **1991**, 21, 987.

(17) Laugier, J.; Bochu, B. *Programme d'affinement des paramètres de maille à partir d'un diagramme de poudre*, Développé au Laboratoire des Matériaux et du Génie Physique, Ecole Nationale Supérieure de Physique de Grenoble (INPG), Domaine Universitaire BP 46, 38402 Saint Martin d'Hères.

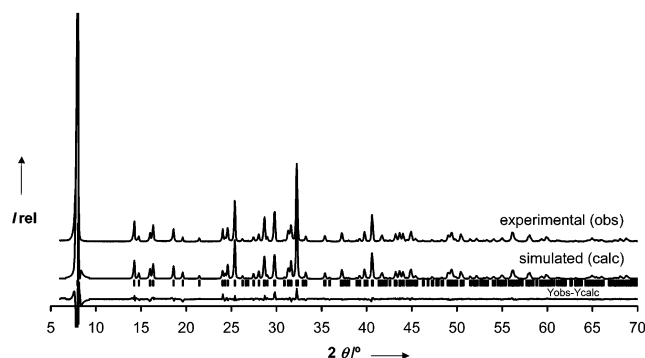
(18) Altomare, A.; Burla, M. C.; Carmalli, M.; Carrozzini, B.; Cascarano, G. L.; Giacovazzo, C.; Guagliardi, A.; Moliterni, A.; Polidori, G.; Rizzi, R. *J. Appl. Crystallogr.* **1999**, 32, 339.

(19) Le Bail, A.; Duroy, H.; Fourquet, J. L. *Math. Res. Bull.* **1988**, 23, 447.

(20) Merlino, S.; Bonaccorsi, E.; Armbruster, T. *Eur. J. Mineral.* **2001**, 13, 577.

Table 1. Conditions of X-ray Data Collection and Refinement for Eu-AV-20, $\text{Na}_{1.08}\text{K}_{0.5}\text{Eu}_{1.14}\text{Si}_3\text{O}_{8.5}\cdot 1.78\text{H}_2\text{O}$

data collection	
diffractometer, geometry	Philips MPD, Bragg–Brentano
radiation	$\text{CuK}\alpha$
2θ range ($^\circ$)	6.01–140.00
step scan	0.03 $^\circ$ (2θ)
time per step	50 s
results of Rietveld refinement in $B11m$ (n 8, setting c2) space group by the FULLPROF program	
cell parameters (\AA)	$a = 6.8309(4)$, $b = 6.8118(4)$, $c = 22.228(1)$, $\gamma = 113.993(3)^\circ$
volume (\AA^3)	944.9(1)
formula units/cell (Z)	4
formula mass (g)	480.7
calculated density (g/cm^3)	3.38
no. of “independent” reflections	990
no. of global refined parameters	4
no. of profile refined parameters	11
no. of intensity-dependent refined parameters	58
global parameters:	
zeropoint	0.014(2)
background polynomial parameters	149(2), $-36(1)$, 4.8(2)
profile parameters:	
Pseudo-Voigt function [$\text{PV} = \eta L + (1-\eta)G$], $\eta = 0.65(1)$	
Caglioti law parameters (U , V , W)	0.128(9), $-0.078(7)$, 0.032(1)
preferred orientation	0.669(2)
asymmetry parameters (up to $45^\circ 2\theta$)	069(7), 0.034(1)
reliability factors (conventional: background excluded)	
for points with Bragg contribution	$R_p = 13.5$, $R_{wp} = 17.0$, $R_{exp} = 7.06$, $\chi^2 = 5.81$
structure reliability factors	$R_B = 7.64$, $R_F = 4.07$

**Figure 1.** Experimental and simulated powder XRD patterns of Eu-AV-20.

program.²¹ The final profile analysis refinement was carried out in the range $13.00\text{--}140.28^\circ 2\theta$ (the region $6.00\text{--}13.00^\circ 2\theta$, where the first peak appears, was excluded due to strong preferential orientation effects) for the occurring 990 “independent” reflections and involved the following: structural parameters—50 fractional atomic coordinates; 7 isotropic temperature factors; profile parameters—one scale factor, one parameter (η) for the pseudo-Voigt peak shape function, three parameters (U , V , W) to describe the angular dependence of the peak full-width-at-half-maximum (fwhm), four unit cell parameters, one parameter for the preferred orientation function (March’s function), two peak asymmetry parameters; global parameters—one zero-point shift, three coefficients of polynomial background. Soft constraints to some of the bond distances were applied.

Table 1 gives the final crystallographic data for Eu-AV-20. The final profile fit is shown in Figure 1, the atomic coordinates are given in Table 2, bond distances and selected bond angles

Table 2. Atomic Coordinates and Equivalent Isotropic Displacement Parameters for Eu-AV-20

name	x	y	z	U_{eq} (\AA^2)	Wyckoff position	occupation
Eu1	0.8239(9)	0.4512(8)	0.20533(6)	0.018(1)	4b	1
Na1	0.313(1)	0.938(1)	0.2061(2)	0.035(1)	4b	0.86
Eu2						0.14
Si1	0.8669(9)	0.9998(8)	0.1544(2)	0.005(1)	4b	1
Si2	0.664(1)	0.608(1)	0.0722(3)	0.005(1)	4b	1
Si3	0.2833(8)	0.3929(8)	0.1557(2)	0.005(1)	4b	1
Na2	0.347(2)	0.674(3)	0	0.690(1)	2a	0.44
Ow3						0.56
K	0.103(2)	0.099(2)	0	0.076(1)	2a	1
O1	0.423(2)	0.544(3)	0.1011(5)	0.026(1)	4b	1
O2	0.092(2)	0.177(2)	0.1301(3)	0.026(1)	4b	1
O3	0.442(2)	0.345(2)	0.2010(3)	0.026(1)	4b	1
O4	0.204(1)	0.539(1)	0.1979(3)	0.026(1)	4b	1
O5	0.655(4)	0.576(6)	0	0.026(1)	2a	1
O6	0.772(5)	0.455(4)	0.0983(3)	0.026(1)	4b	1
O7	0.805(3)	0.858(2)	0.0934(3)	0.026(1)	4b	1
O8	0.712(1)	0.071(1)	0.1954(3)	0.026(1)	4b	1
O9	0.914(2)	0.824(2)	0.1927(4)	0.026(1)	4b	1
Ow1	0.964(2)	0.443(2)	0	0.217(6)	2a	1
Ow2	0.274(8)	0.879(6)	0.0812(5)	0.217(6)	4b	1

are collected in Tables 3 and 4, respectively. The lattice parameters for Ce-, Sm-, Tb-AV-20, and for the mixed Eu/Tb- and Tb/Gd-AV-20 are given in Table 5. Bond valence calculations are given in Table 1 of Supporting Information. Estimated values are close to the formal values.

The structure of Eu-AV-20 is closely related with the structure of tobermorite 11 \AA minerals (hydrated calcium silicates).²⁰ A common feature of the tobermorite family is the layer built up by seven-coordinated (mono-capped trigonal prisms) calcium cations. In AV-20 the substitution $2\text{Ca}^{2+} \leftrightarrow \text{Eu}^{3+} + \text{Na}^+$ occurs, with Eu^{3+} and Na^+ being seven-coordinated (Figure 2a). In addition some (ca. 10%) Eu^{3+} ions are disordered over the Na^+ sites. Columns of $\text{Eu}^{3+}/\text{Na}^+$ polyhedra run along the $[110]$ direction and neighboring columns in each layer present the

(21) Rodríguez-Carvajal, J. FULLPROF Program for Rietveld Refinement and Pattern Matching Analysis; Abstracts of the Satellite Meeting on Powder Diffraction of the XVth Congress of the International Union of Crystallography, Toulouse, France, 1990, p 127.

Table 3. Selected Bond Distances (Å) for Eu-AV-20

bond	distance	bond	distance	bond	distance
Eu1–O3	2.411(14)	Si1–O2	1.614(14)	Na2–O1	2.545(15)
Eu1–O3	2.447(10)	Si1–O7	1.619(10)	Na2–O1	2.545(15)
Eu1–O4	2.419(12)	Si1–O8	1.611(10)	Na2–O5	2.455(37)
Eu1–O4	2.462(9)	Si1–O9	1.603(12)	Na2–Ow1	2.443(23)
Eu1–O6	2.407(9)			Na2–Ow2	2.452(34)
Eu1–O8	2.396(9)	Si2–O1	1.654(16)	Na2–Ow2	2.452(34)
Eu1–O9	2.377(11)	Si2–O5	1.618(8)		
		Si2–O6	1.615(31)	K–O2	2.946(8)
Na1–O3	2.546(14)	Si2–O7	1.646(13)	K–O2	2.946(8)
Na1–O4	2.515(11)			K–O7	2.905(15)
Na1–O8	2.510(12)	Si3–O1	1.626(16)	K–O7	2.905(15)
Na1–O8	2.568(10)	Si3–O2	1.622(14)	K–Ow1	2.865(20)
Na1–O9	2.530(17)	Si3–O3	1.607(12)	K–Ow2	2.882(40)
Na1–O9	2.562(12)	Si3–O4	1.615(10)	K–Ow2	2.882(40)
Na1–Ow2	2.802(14)				

capping ligands (water molecules and oxygen atoms) on their opposite surfaces. In mixed lanthanide samples, these columns seem to have enough structural flexibility to host, at least, two different ions, such as Eu^{3+} and Tb^{3+} or Gd^{3+} and Tb^{3+} .

The silicate chains in tobermorites are of the wollastonite type and run along the [110] direction, on both sides of the $\text{Eu}^{3+}/\text{Na}^+$ containing layers, shifted by $(\mathbf{a}+\mathbf{b})/4$. These chains

are built up of Si_2O_7 units (paired Si1 and Si3 centered tetrahedra) which link through a bridging (Si2 centered) tetrahedron (Figure 2b). Two wollastonite-type chains lying on the symmetry plane normal to \mathbf{c} are condensed through the bridging oxygen O5, forming a double silicate chain normal to [1–10]. In this way, eight-member rings are formed. Each siliceous chain connects to a column of calcium polyhedra by Si_2O_7 units sharing the oxygen atoms of the edges opposite to the capping ligands. The bridging tetrahedron shares the capping O6 ligand of the neighboring columns. Successive tetrahedral chains (and, thus, the double chains) on one side of the layer are shifted by $(\mathbf{a} + \mathbf{b})/2$.

Eu/Na polyhedra layers are connected through double silicate chains, building up a framework with channels running along the [110] direction. These channels may also be accessed through the double silicate chains 8-membered rings.

The cavities of Eu-AV-20 contain Na^+ and K^+ ions at a special position 2a. The latter is seven-coordinated to four framework oxygen atoms and three water molecules, whereas Na is six-coordinated to three framework oxygen atoms and three water molecules. Both sites (particularly the Na site) may be partially occupied by water molecules (Figure 2c).

Table 4. Selected Bond Angles for Eu-AV-20

bond	angle (deg)	bond	angle (deg)	bond	angle (deg)
O3–Eu1–O3	113.0(7)	O2–Si1–O7	96.0(11)	O1–Na2–O1	124.0(8)
O3–Eu1–O4	173.1(9)	O2–Si1–O8	120.5(11)	O1–Na2–O5	65.6(11)
O3–Eu1–O4	71.4(5)	O2–Si1–O9	108.4(11)	O1–Na2–Ow1	95.3(9)
O3–Eu1–O6	79.6(9)	O7–Si1–O8	127.5(10)	O1–Na2–Ow2	70.4(16)
O3–Eu1–O8	80.8(6)	O7–Si1–O9	94.7(9)	O1–Na2–Ow2	164.8(17)
O3–Eu1–O9	95.5(7)	O8–Si1–O9	106.2(10)	O1–Na2–O5	65.6(11)
O3–Eu1–O4	71.5(5)			O1–Na2–Ow1	95.3(9)
O3–Eu1–O4	60.7(5)	O1–Si2–O5	111.8(14)	O1–Na2–Ow2	164.8(17)
O3–Eu1–O6	155.7(8)	O1–Si2–O6	111.2(25)	O1–Na2–Ow2	70.4(16)
O3–Eu1–O8	75.9(5)	O1–Si2–O7	105.1(15)	O5–Na2–Ow1	129.6(19)
O3–Eu1–O9	116.4(7)	O5–Si2–O6	105.8(19)	O5–Na2–Ow2	123.3(26)
O4–Eu1–O4	115.5(6)	O5–Si2–O7	113.3(16)	O5–Na2–Ow2	123.3(26)
O4–Eu1–O6	94.4(11)	O6–Si2–O7	109.7(21)	Ow1–Na2–Ow2	87.4(15)
O4–Eu1–O8	95.7(5)			Ow1–Na2–Ow2	87.4(15)
O4–Eu1–O9	86.7(7)	O1–Si3–O2	111.2(15)	Ow2–Na2–Ow2	94.8(13)
O4–Eu1–O6	142.9(6)	O1–Si3–O3	109.1(12)		
O4–Eu1–O8	110.7(5)	O1–Si3–O4	107.5(11)	O2–K–O2	157.9(5)
O4–Eu1–O9	79.1(5)	O2–Si3–O3	113.2(12)	O2–K–O7	48.5(4)
O6–Eu1–O8	86.3(8)	O2–Si3–O4	114.5(10)	O2–K–O7	137.8(6)
O6–Eu1–O9	81.3(8)	O3–Si3–O4	100.7(10)	O2–K–Ow1	79.2(6)
O8–Eu1–O9	167.5(7)			O2–K–Ow2	61.6(13)
		Si2–O1–Si3	136.1(10)	O2–K–Ow2	138.9(13)
O3–Na1–O4	172.8(8)	Si1–O2–Si3	137.0(9)	O2–K–O7	137.8(6)
O3–Na1–O8	76.1(6)	Eu1–O3–Eu1	108.9(5)	O2–K–O7	48.5(4)
O3–Na1–O8	71.2(5)	Eu1–O3–Si3	134.5(7)	O2–K–Ow1	79.2(6)
O3–Na1–O9	100.3(8)	Eu1–O3–Na1	100.3(6)	O2–K–Ow2	138.9(13)
O3–Na1–O9	110.6(7)	Eu1–O4–Eu1	108.1(5)	O2–K–Ow2	61.6(13)
O3–Na1–Ow2	94.7(11)	Eu1–O4–Si3	118.9(6)	O7–K–O7	91.3(5)
O4–Na1–O8	100.6(5)	Eu1–O4–Na1	94.6(5)	O7–K–Ow1	94.3(7)
O4–Na1–O8	116.0(5)	Si2–O5–Si2	165.9(7)	O7–K–Ow2	66.3(15)
O4–Na1–O9	81.4(7)	Eu1–O6–Si2	117.9(12)	O7–K–Ow2	119.6(16)
O4–Na1–O9	74.7(5)	Si1–O7–Si2	139.3(8)	O7–K–Ow1	94.3(7)
O4–Na1–Ow2	78.7(9)	Eu1–O8–Si1	114.7(5)	O7–K–Ow2	119.6(16)
O8–Na1–O8	111.2(6)	Eu1–O8–Na1	101.7(5)	O7–K–Ow2	66.3(15)
O8–Na1–O9	167.4(9)	Na1–O8–Na1	101.5(5)	Ow1–K–Ow2	139.9(20)
O8–Na1–O9	78.8(5)	Eu1–O9–Si1	144.7(7)	Ow1–K–Ow2	139.9(20)
O8–Na1–Ow2	89.0(13)	Eu1–O9–Na1	103.6(5)	Ow2–K–Ow2	77.6(12)
O8–Na1–O9	78.3(6)	Na1–O9–Na1	101.2(6)		
O8–Na1–O9	60.1(5)				
O8–Na1–Ow2	150.7(9)				
O9–Na1–O9	113.6(8)				
O9–Na1–Ow2	79.2(12)				
O9–Na1–Ow2	148.0(9)				

Table 5. Unit Cell Parameters of AV-20 Materials

	<i>a</i> (Å)	<i>b</i> (Å)	<i>c</i> (Å)	γ (°)	volume (Å ³)
Ce-AV-20	6.875(1)	6.824(1)	22.099(1)	114.16(1)	948.2(3)
Sm-AV-20	6.840(1)	6.819(1)	22.220(1)	114.13(1)	945.8(1)
Tb-AV-20	6.813(2)	6.773(2)	22.055(7)	113.99(1)	929.6(4)
Eu/Tb-AV-20	6.823(1)	6.808(1)	22.204(4)	113.97(1)	942.5(2)
Tb/Gd-AV-20	6.781(1)	6.766(1)	22.169(4)	113.80(1)	930.7(4)

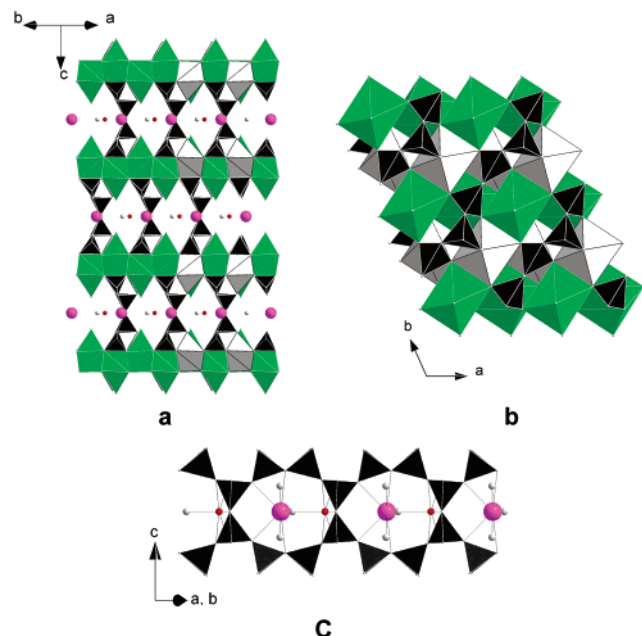


Figure 2. (a) Crystal structure of Eu-AV-20; (b) Connection of silicate chains to the layer of EuO₇ and NaO₇ polyhedra; (c) Schematic representation of the K⁺ and Na⁺ ions residing in the pores of Eu-AV-20. K⁺ is seven-coordinated to four framework oxygen atoms and three water molecules, whereas Na⁺ is six-coordinated to three framework oxygen atoms and three water molecules. Polyhedra: green (EuO₇), white/light gray (NaO₇), black (SiO₄); spheres: purple (KO₄(H₂O)₃), red (NaO₃(H₂O)₃), light gray (H₂O).

Tobermorites 11 Å are known as “anomalous” or “normal”, respectively, depending on whether they transform into tobermorites 9 Å upon heating at ca. 300 °C.²⁰ In addition, “anomalous” tobermorites contain only zeolitic water molecules while in ‘normal’ tobermorites there are also Ca²⁺ ions in the cavities. Eu-AV-20 is unusual because it contains large amounts of cations in the cavities and its structure does not transform upon calcination up to 800 °C.

Due to the paramagnetism of Eu³⁺ and Ce³⁺ ions, it was not possible to obtain a ²⁹Si MAS NMR spectrum of acceptable quality of Eu- and Ce-AV-20. Because Sm³⁺ is less paramagnetic the ²⁹Si MAS NMR spectrum of Sm-AV-20 (Figure 3) was measured, and it displays three resonances at −74.3, −82.9, and −88.9 ppm on a 1:1:1 ratio. This is in accord with the XRD crystal structure, which calls for three nonequivalent Si sites with equal populations.

The ²³Na MAS NMR spectra of Eu- and Ce-AV-20 materials exhibit two NMR resonances at, respectively, ca. 4 and −75 ppm and 3.5 and −9 ppm (Figure 4). The peaks at −75 and −9 ppm are strongly shifted and exhibit intense spinning sidebands and are, thus, assigned to ²³Na nuclei interacting with paramagnetic Eu³⁺/Ce³⁺ ions in the layers. The resonances at high frequency are attributed to the Na⁺ ions in the cavities. These assignments are supported by the ²³Na MAS NMR spectrum of Sm-AV-20: because of the relatively low Sm³⁺

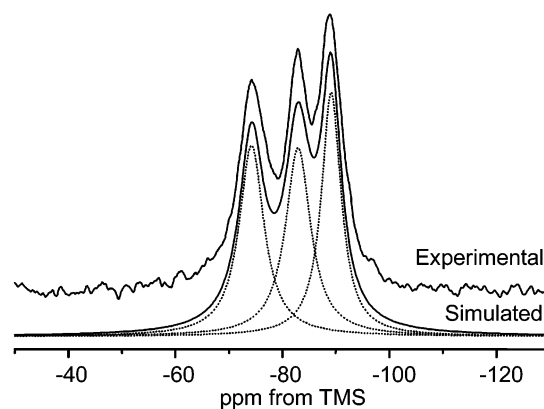


Figure 3. Experimental and simulated ²⁹Si MAS NMR spectrum of Sm-AV-20.

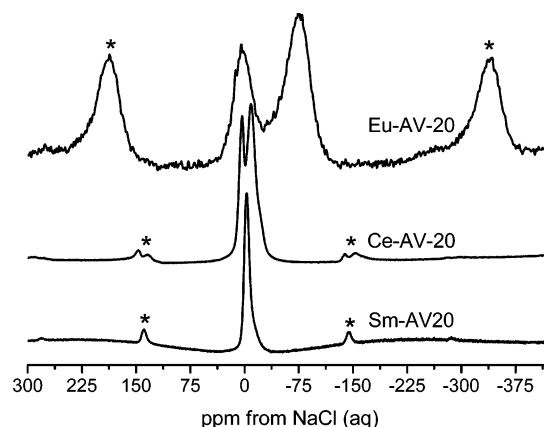


Figure 4. Single-quantum ²³Na MAS NMR spectra of AV-20 materials. Asterisks depict spinning sidebands.

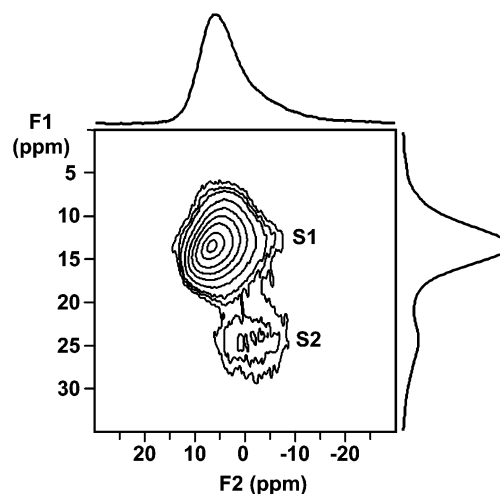


Figure 5. Triple-quantum ²³Na MAS NMR spectrum of Sm-AV-20. The horizontal F2 projection is similar to the ‘conventional’ MAS NMR spectrum, while the isotropic F1 projection reveals the presence of two Na resonances.

paramagnetism, the resonances given by Na⁺ ions in the layers and in the cavities overlap (peak at −3 ppm) and can only be resolved by ²³Na 3Q MAS NMR (Figure 5).

Simulations of the single- and triple-quantum MAS NMR spectra (not shown) reveal that these two peaks are in a ca. 4:1 ratio. The obtained (average) isotropic chemical shift and quadrupole coupling constant (assuming $\eta = 0.65$) for the resonances attributed to Na⁺ ions in layers (S1) and in the

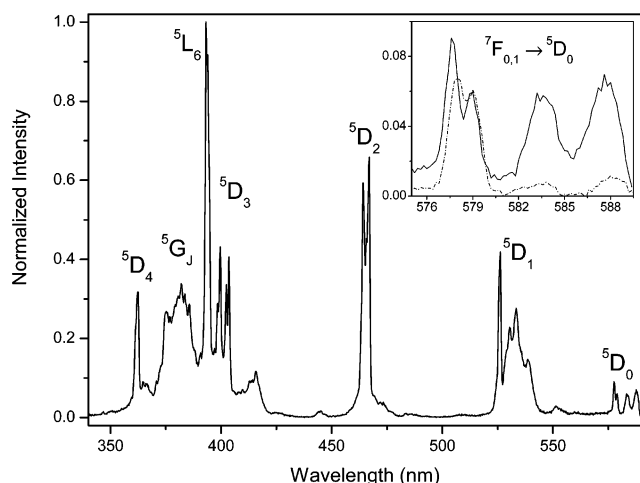


Figure 6. Excitation spectrum of Eu-AV-20 detected within the strongest 7F_2 manifold (611.5 nm) at RT. The inset shows the ${}^7F_{0,1} \rightarrow {}^5D_0$ transitions at 300 (solid line) and 10 K (dashed line).

cavities (S2) are, respectively, $\delta_{\text{iso}} = 10.5$ and 14.5 ppm and $C_Q = 1.45$ and 2.55 MHz. There is a significant distribution of isotropic chemical shifts for both sites, particularly for S2 (4 and 2.5 ppm, for S2 and S1, respectively), and a relatively small distribution of quadrupole couplings (0.15 MHz). Integration of the Eu-AV-20 spectrum also yields a population ratio (Na^+ ions in the layers/cavities) of ca. 4, in good agreement with the powder XRD refinement, which gives a population ratio of only 3.9.

The room-temperature (RT) excitation spectrum of as-prepared (hydrated) Eu-AV-20 (Figure 6) displays a series of sharp lines assigned to ${}^7F_{0-1} \rightarrow {}^5D_{4-0}$, 5L_6 , and 5G_J transitions. The inset details the ${}^7F_{0,1} \rightarrow {}^5D_0$ region, recorded at RT and 10 K. The latter, in particular, clearly show the presence of two ${}^7F_0 \rightarrow {}^5D_0$ transitions (at ca. 578–579 nm) that are unequivocally ascribed to two different Eu^{3+} sites. One of these sites corresponds to Eu^{3+} in regular positions in the Eu/Na polyhedra layers (Eu1), whereas the other site is probably associated with Eu^{3+} ions, which are disordered over the Na^+ sites (Eu2). At RT, the two other lines in the spectrum appearing at high wavelengths (ca. 583–588 nm) are attributed to the ${}^7F_1 \rightarrow {}^5D_0$ transitions.

The RT emission spectra of as-prepared Eu-AV-20 are shown in Figure 7. The sharp emission lines are assigned to transitions between the first excited nondegenerate 5D_0 state and the ${}^7F_{0-4}$ levels of the fundamental Eu^{3+} septet. Luminescence from higher excited states, such as 5D_1 , is not detected indicating very efficient nonradiative relaxation to the 5D_0 level. Except for the ${}^5D_0 \rightarrow {}^7F_1$ lines, which have a predominant magnetic dipole character, the observed transitions are mainly of electric dipole nature. In accord with the evidence provided by the excitation spectrum, two local Eu^{3+} environments are clearly inferred from the presence of two ${}^5D_0 \rightarrow {}^7F_0$ lines (inset of Figure 7). Moreover, the observed splitting of the ${}^7F_{1,2}$ levels (4 and 7 Stark components levels, respectively) corroborates the existence of two local Eu environments. The occurrence of the ${}^5D_0 \rightarrow {}^7F_{0,3}$ transitions and the J-degeneracy of the ${}^7F_{1,2}$ levels indicate that the point symmetry group of Eu^{3+} ions is consistent with the crystallographic $B11m$ space group (C_s in Schoenflies

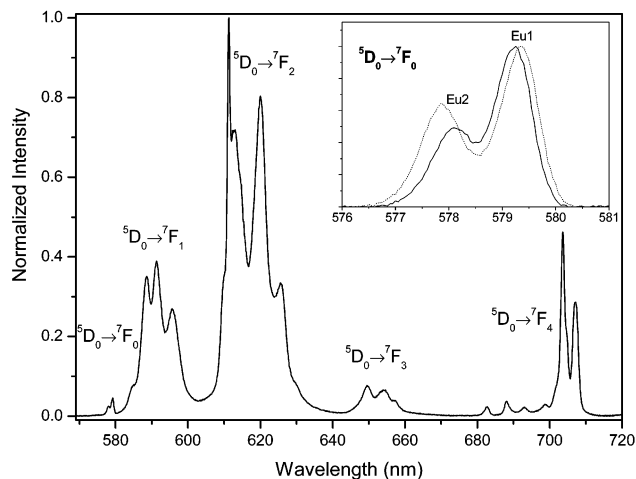


Figure 7. RT emission spectra of Eu-AV-20 excited at 394 nm. The inset shows the ${}^5D_0 \rightarrow {}^7F_0$ transition recorded at ambient pressure (solid line) and under vacuum after ca. 20 h (dashed line).

notation) (ref 22 and refs therein). In general, when two lanthanide local sites are present, photoluminescence measurements do not allow a quantitative determination of their relative populations because the absorption cross-sections may be different or distinct nonradiative deactivations occur. Indeed, the spectrum in Figure 7 yields relative populations of 60 (Eu1) and 40% (Eu2), in contrast with the 90 (Eu1) and 10% (Eu2) obtained from the structural analysis.

The relative intensities of two ${}^5D_0 \rightarrow {}^7F_0$ lines change with the time of exposure to vacuum (ca. 10^{-3} – 10^{-4} N·m $^{-2}$) (inset in Figure 7). There is also a slight variation in the energy of these lines: the high-energy transition blue-shifts 6.7 cm^{-1} , whereas the energy of the other transition red-shifts only slightly, ca. 2.9 cm^{-1} (we note that the resolution of the photoluminescence measurements is ca. 1.5 cm^{-1}). The Eu2 ions, which are disordered over the Na1 sites, are expected to be more sensitive to vacuum exposure (there is a water molecule ca. 2.8 Å away from the Na1 site; this compares with a typical Eu–O bond distance of ca. 2.4 Å) and, therefore, the ${}^5D_0 \rightarrow {}^7F_0$ high-energy line should correspond to this site. In addition, the fwhm of this line, ca. 27 cm^{-1} , is larger than the fwhm (ca. 20 cm^{-1}) of the lower-energy transition. This is to be expected because this Eu2 site exhibits a larger dispersion of local environments. From the powder XRD pattern (not shown) of the Eu-AV-20 sample calcined in situ, under vacuum, at 400 °C the following lattice parameters were determined: $a = 6.716(2)$, $b = 6.670(2)$, $c = 22.121(7)$ Å, $\gamma = 113.2882$. Thus, upon dehydration there is no phase transformation, only shrinkage of the unit cell, whose volume decreases from 944.9 to 910.3 Å 3 . It is possible that this cell shrinkage brings about slight changes in the local environments of Eu1 and Eu2, which also contribute to the subtle energy shifts observed.

The two Eu^{3+} sites have similar lifetimes, not distinguishable with our experimental set up. The 5D_0 decay curves detected within the ${}^5D_0 \rightarrow {}^7F_0$ region at two distinct wavelengths associated with the Eu1 and Eu2 local sites are well fitted by an exponential function, yielding similar lifetime values of ca. 1.66 and 1.68 (± 0.02) ms (not shown). Furthermore, the 5D_0 decay curves recorded monitoring the ${}^5D_0 \rightarrow {}^7F_1$ and ${}^5D_0 \rightarrow$

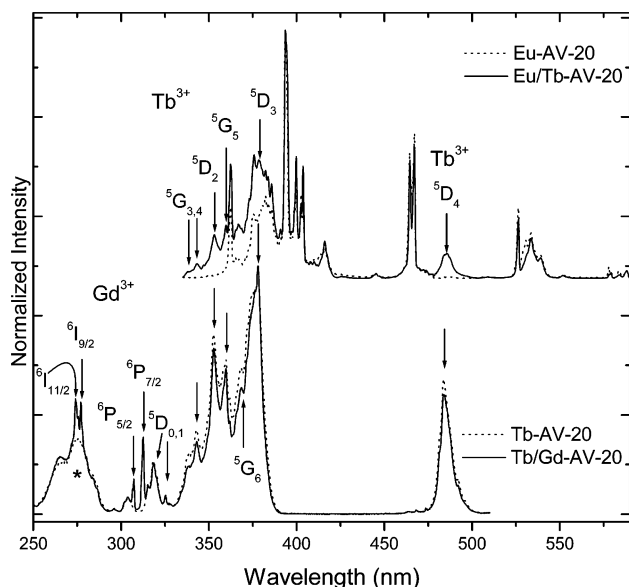


Figure 8. RT excitation spectra of Eu-AV-20 and Eu/Tb-AV-20, Tb-AV-20 and Tb/Gd-AV-20, monitored at the $^5D_0 \rightarrow ^7F_2$ (611 nm) and $^5D_4 \rightarrow ^7F_5$ (541 nm) transitions, respectively. The arrows indicate the $^5D_{4-0}$, $^5G_{6-3}$ Tb^{3+} and $^6P_{7/2,5/2}$, $^6I_{9/2,11/2}$ Gd^{3+} levels. The asterisk in the spectra of Tb-AV-20 and Tb/Gd-AV-20 indicates a ligands-to-metal charge-transfer band.

7F_2 transitions are also well fitted by a single-exponential function, indicating that the lifetimes of the Eu^{3+} local sites are, indeed, undistinguishable. The obtained values are analogous to those detected within the $^5D_0 \rightarrow ^7F_0$ region indicating similar contributions of the two local sites for the decay curves. Time-resolved spectra recorded at different delay times further confirm the similarity of the lifetimes of the two Eu^{3+} sites. Indeed, no differences were found in the relative intensity of both the two $^5D_0 \rightarrow ^7F_0$ lines and the remaining $^5D_0 \rightarrow ^7F_{1,2}$ transitions as the delay time increases from 0.08 to 4.00 ms (not shown).

Figure 8 compares the excitation spectra of Eu-AV-20 and Eu/Tb-AV-20, Tb-AV-20 and Tb/Gd-AV-20, monitored within the $Eu^{3+} \ ^5D_0 \rightarrow ^7F_2$ (611 nm) and $Tb^{3+} \ ^5D_4 \rightarrow ^7F_5$ (541 nm) transitions, respectively. The spectrum of Eu/Tb-AV-20 exhibits the $^5D_{4-0}$ and $^5G_{6-3}$ Tb^{3+} levels, while the spectrum of Tb/Gd-AV-20 displays the $^6P_{7/2,5/2}$ and $^6I_{9/2,11/2}$ Gd^{3+} levels. This evidence clearly shows the occurrence of energy transfer from Tb^{3+} to Eu^{3+} (Eu/Tb-AV-20) and Gd^{3+} to Tb^{3+} (Tb/Gd-AV-20).

The emission spectra of Eu/Tb-AV-20 and Tb/Gd-AV-20 excited in the Tb^{3+} (378 nm) and Gd^{3+} (313 nm) levels (Figure 9) show the typical Eu^{3+} and Tb^{3+} lines, which appear in the spectra of Eu-AV-20 and Tb-AV-20 materials. Similar spectra were obtained for Eu/Tb-AV-20 under excitations within other

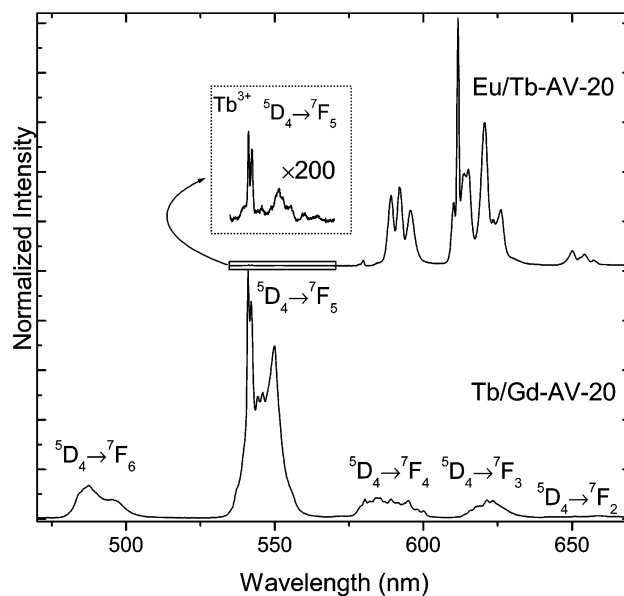


Figure 9. Emission spectra (300 K) of Eu/Tb-AV-20 and Tb/Gd-AV-20 excited at 378 (5D_3 Tb^{3+} level) and 313 ($^6P_{7/2}$ Gd^{3+} level) nm, respectively. The inset in the spectrum of the former sample shows a vertical expansion of the $Tb^{3+} \ ^5D_4 \rightarrow ^7F_5$ transition.

Tb^{3+} levels (485 nm, 5D_4) which do not overlap with Eu^{3+} states. This supports the above-mentioned energy transfer between lanthanide ions. The fact that this energy transfer occurs clearly indicates that the two kinds of lanthanide optical centers are in close spatial proximity (that is, for example, there is no clustering of a given lanthanide in a separate crystal domain).

In conclusion, a novel and promising microporous lanthanide silicate system, exhibiting interesting photoluminescence properties, with a structure closely related with the structure of mineral tobermorites has been reported. The structural flexibility of these materials allows fine-tuning of luminescence properties, by introducing a second type of lanthanide ion in the framework. Together with previous work, this indicates that a range of other microporous stoichiometric lanthanide silicates with luminescence properties will be prepared soon.

Acknowledgment. We thank FCT, POCTI, and FEDER for financial support.

Supporting Information Available: Further details on the crystal structure investigation may be obtained from the Fachinformationzentrum Karlsruhe, D-76344 Eggenstein-Leopoldshafen, Germany (e-mail: crysdata@fiz-karlsruhe.de) on quoting the depository CSD number 413231. Bond valence calculations are given in Table 1 of Supporting Information.

JA036988P